Chemical Science

ROYAL SOCIETY OF CHEMISTRY

EDGE ARTICLE

View Article Online
View Journal | View Issue

Cite this: *Chem. Sci.*, 2026, **17**, 6593

All publication charges for this article have been paid for by the Royal Society of Chemistry

Received 27th November 2025
Accepted 23rd January 2026

DOI: 10.1039/d5sc09295g

rsc.li/chemical-science

Synergistic strategy of interfacial ion channels and a cross-linked network in a composite electrolyte for dendrite-free sodium-metal batteries

Lei Zhai,[a] Hanghang Dong,[b] Haichao Wang,[d] Yijie Duan,[a] Zuo Liu,[a] Shuang Yan,[a] Chenguang You,[a] Hao Yan,[d] Xin Tan[a] and Shuangqiang Chen *[cd]

Solid-state electrolytes (SSEs) can address the safety concerns of liquid electrolytes in sodium-metal batteries, but their low ionic conductivity and high interfacial resistance limit practical use. To tackle these problems, this study develops a flexible and tunable composite solid electrolyte (CSE) by integrating $Na_3Zr_2Si_2PO_{12}$ (NZSPO) active fillers into a polymer matrix that combines the high dielectric constant of polyacrylonitrile (PAN) with an interpenetrating and cross-linked polyethylene oxide (PEO) network. The resulting electrolyte achieved a high Na^+ transference number of 0.64 and an exceptional ionic conductivity of >1.2 × 10^{-3} S cm^{-1} at 30 °C. It enabled stable Na plating/stripping for over 2500 hours in symmetric cells, and when paired with a $Na_3V_2(PO_4)_3$ (NVP) cathode, delivered outstanding cycling stability (95.2 mAh g^{-1} after 500 cycles at 0.5C) with an ultra-low decay rate of 0.029% per cycle due to the good interface contact based on the good external flexibility and high internal mechanical stability of the composite solid electrolyte. Theoretical calculation has demonstrated that Na^+ cations have low transferring energy barriers in both NZSPO particles and the polymer matrix. The work highlights a synergistic filler–polymer strategy for advancing solid-state batteries.

Introduction

The rapid growth of consumer electronics and electric vehicles is driving the pursuit of advanced energy storage systems that simultaneously combine high energy density, cost-effectiveness, and intrinsic safety.[1–4] Solid-state batteries (SSBs) have emerged as a transformative alternative to conventional liquid-electrolyte-based lithium-ion systems, particularly with the ongoing shift toward sodium-based chemistry for enhanced sustainability and resource availability.[5–8] By replacing flammable organic liquids with solid electrolytes (SEs),[9–12] SSBs fundamentally eliminate leakage and combustion risks while enabling the integration of high-voltage cathodes and metallic anodes, which is a critical step toward achieving energy densities exceeding 400 Wh kg^{-1}.[13–15] Notably, sodium-based systems present compelling advantages compared to their lithium counterparts, such as substantially lower material costs, superior thermal stability and reduced reactivity.[16–18] Despite these merits, the practical realization of solid-state sodium batteries remains hampered by critical challenges, particularly in electrolyte design.[19,20]

Solid electrolytes, serving as the core components of solid-state sodium-metal batteries, are generally categorized into three main classes: inorganic, polymer, and composite systems.[21,22] Inorganic solid electrolytes (ISEs), such as oxide-type (*e.g.*, sodium super ionic conductor (NASICON)-type $Na_3Zr_2Si_2PO_{12}$, NZSPO), typically exhibit high mechanical strength (>1.0 GPa), wide electrochemical windows (>4.5 V), and excellent chemical stability.[23,24] Furthermore, compared to the widely studied NZSPO materials, other oxide solid-state electrolytes need to further enhance their ionic conductivity. For instance, Yang *et al.* increased the sodium vacancies in $Na_5YSi_4O_{12}$ by replacing Y^{3+} with Zr^{4+}, thereby introducing ample sodium vacancies. Combined with the local chemical environment alteration by Zr^{4+}, the conductivity of the material was improved to 3.3 mS cm^{-1}, and the critical current density reached 2.4 mA cm^{-2}. However, their practical deployment is often constrained by the complex synthesis processes (*e.g.* sintering temperatures >1200 °C) and high interfacial impedance.[25–27] Sulfide-based ISEs (*e.g.*, Na_3PS_4) can achieve ultra-high ionic conductivity (>1.0 mS cm^{-1}), especially in the highly promising electrolyte $Na_{11}Sn_2PS_{12}$, where a value of 1.4 mS cm^{-1} can be achieved. In addition, halide modification can be carried out on the basis of sulfide. Dong *et al.* constructed a kind of Na–Zr–S–Cl SSE (Na_2S-$1.3ZrCl_4$) with a rich chlorine structure. By precisely tuning the

[a]*College of Chemistry and Materials Engineering, Wenzhou University, Wenzhou, Zhejiang 325035, China*

[b]*School of Energy and Power Engineering, Nanjing University of Science and Technology, Nanjing, 210094, China*

[c]*State Key Laboratory of Advanced Fiber Materials, College of Materials Science and Engineering, Donghua University, Shanghai 201620, China. E-mail: chensq@dhu.edu.cn*

[d]*Department of Chemical Engineering, School of Environmental and Chemical Engineering, Shanghai University, Shangda Road 99, Shanghai 200444, China*

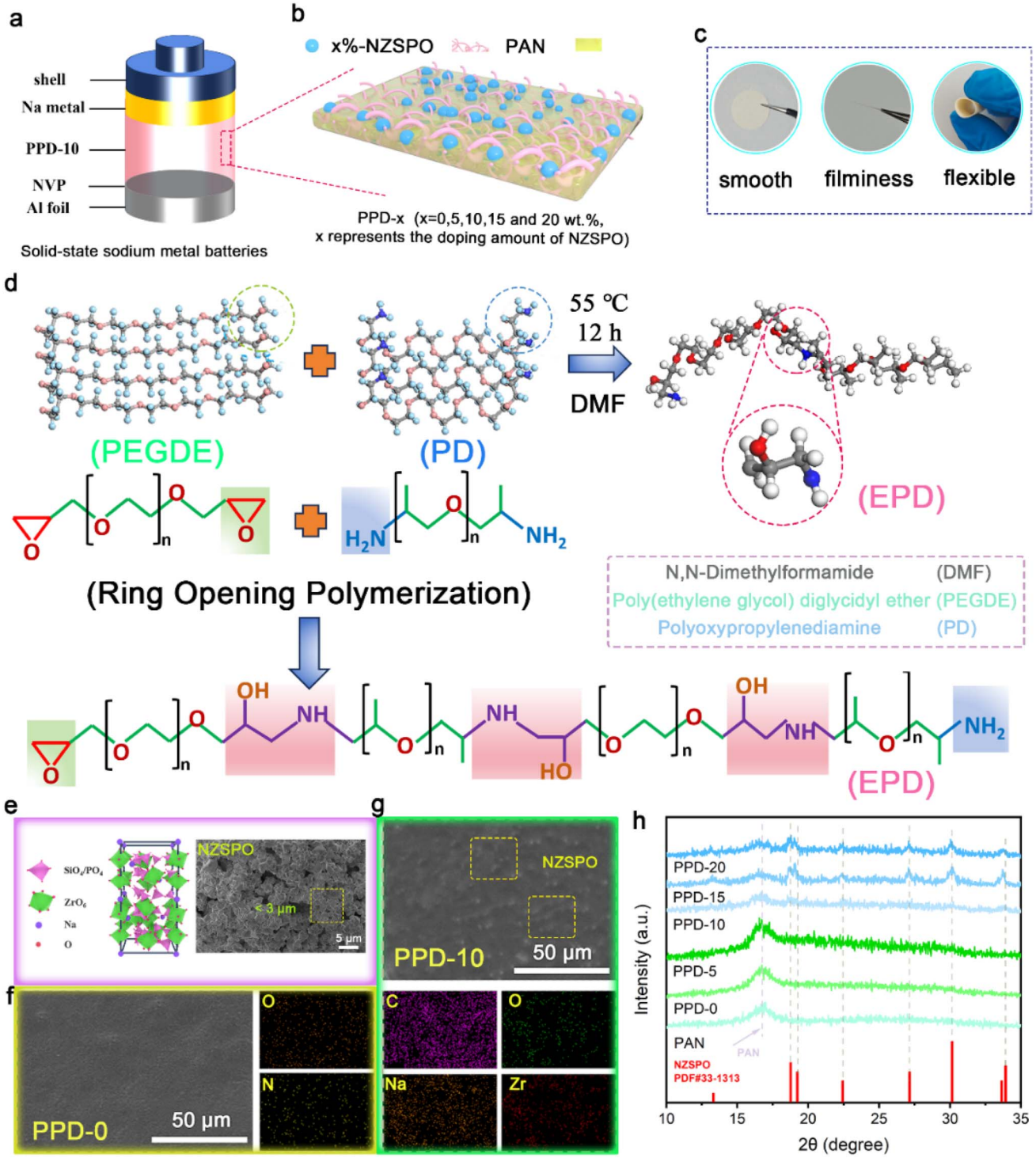

Fig. 1 Schematic illustration and structural characterization of the composite solid electrolyte design. (a) Configuration of a solid-state sodium-metal battery; (b) schematic diagram of the proposed composite solid electrolyte; (c) digital photograph of the flexible electrolyte film; (d) reaction scheme for the epoxy-amine ring-opening polymerization; (e) crystal structure (top) and the corresponding SEM image (bottom) of the NASICON-type NZSPO filler; scanning electron microscope images and elemental mapping of (f) PPD-0 and (g) PPD-10 electrolyte films; (h) XRD patterns of composite electrolytes with varying NZSPO content.

S^{2-}/Cl^{-} ratio, the Na_2S-1.3$ZrCl_4$ SSE was successfully prepared, exhibiting superior thermal stability and mechanical properties. Nevertheless, sulfide-based SSEs generally suffer from poor chemical stability and are prone to react with ambient moisture, releasing toxic gases, a key limitation that hinders their practical application.[28–30] While borohydride ISEs possess intrinsic safety, they also suffer from the insufficient room-temperature ionic conductivity ($<10^{-4}$ S cm^{-1}). A further common

drawback of ISEs is the requirement for thick layers (>200 μm) to ensure mechanical integrity, which inevitably compromises cell-level energy density.[31,32] By contrast, solid polymer electrolytes (SPEs), such as poly(ethylene oxide) (PEO), enable thin configurations (<100 μm) and improved interfacial compatibility with electrodes.[33–35] Nevertheless, their low ionic conductivity at room temperature (10^{-8}–10^{-6} S cm^{-1}) and insufficient mechanical strength (Young's modulus <10 MPa) often lead to the dendrite penetration and thermal softening issues.[36–38]

Composite solid-state electrolytes generally refer to hybrid systems consisting of a polymer matrix and inorganic fillers, aiming to combine the flexibility of polymers with the high ionic conductivity and mechanical stability of inorganic materials.[39–41] In current research, the mainstream approach involves incorporating inert inorganic fillers (*e.g.*, SiO_2 and La_2O_3) into single-phase polymer matrices (such as poly(-ethylene oxide) or poly(vinylidene fluoride)) to improve mechanical properties and interfacial stability.[42,43] However, such strategies still face several challenges:[44–48] firstly, limited compatibility between inert fillers and the polymer matrix often leads to increased interfacial resistance and non-uniform ion transport. Secondly, poor dispersion of fillers tends to cause aggregation, compromising structural homogeneity. Thirdly, most fillers exhibit limited direct contribution to lithium-ion migration, making it difficult to achieve significant enhancement in ionic conductivity. Regarding the aforementioned issues, recent research has focused on advanced engineering strategies to overcome these limitations:[49,50] (i). chemical modification: constructing crosslinked networks (*e.g.*, PAN-*co*-polyamine) functionalized with polar groups (*e.g.*, cyano and CN) to weaken Na^+–polymer interactions, thereby improving oxidative stability (>4.3 V) and Na^+ transport efficiency (conductivity: $\sim 1.2 \times 10^{-4}$ S cm^{-1}).[51,52] (ii) Filler engineering: employing surface-functionalized NASICON particles (*e.g.*, SiO_2-coated) to mitigate agglomeration and establish uniform percolation networks for good ion conduction.[53,54] (iii) Hybrid architectures: designing thin-film CSEs (<50 μm) that combining nano-sized fillers (*e.g.*, Al_2O_3) with copolymers (*e.g.*, PVDF-HFP) to achieve a balance between mechanical strength (modulus >50 MPa) and ionic conductivity (5×10^{-4} S cm^{-1}).[55]

Guided by the above considerations, we herein report a novel composite solid electrolyte engineered through a multi-component design strategy. The CSE film has a flexible, three-dimensional feature, integrating NASICON-type $Na_3Zr_2Si_2PO_{12}$ (NZSPO) active fillers into a polymer matrix that combines the high dielectric constant of polyacrylonitrile (PAN) with an interpenetrating, cross-linked polyethylene oxide (PEO) network, synthesized *via* a ring-opening polymerization between amine (–NH_2) and epoxy (–C_2H_3O) groups (Fig. 1a and b). The key difference from previous studies lies in the fact that it is not a simple physical mixture of a single polymer and inorganic materials. Instead, cross-linking polymerization between polymers was achieved through chemical reactions, and the components of a single polymer were broken down. PAN with a high dielectric constant was added as a polymer filler, and the addition of active filler NZSPO also played a role, working together to enhance the performance of the material. The synthesized free-standing electrolyte film (Fig. 1c) exhibits a smooth morphology, tunable thickness, and remarkable flexibility, ensuring compatibility with diverse battery configurations. As illustrated in Fig. 1d and S2a, the integrated PAN and polyethylene glycol diglycidyl ether (PEGDE)/poly-oxypropylenediamine (PD) (marked as EPD) framework creates a highly cross-linked network (labeled as PPD). The abundant N-sites on the electrolyte surface serve as effective coordination centers for Na^+, while the rigid, cross-linked structure decouples ion transport from the segmental dynamics of the polymer chain. This synergy facilitates rapid Na^+ diffusion through a thermodynamically favorable pathway, rather than relying solely on chain-assisted hopping. Furthermore, the incorporation of NASICON-type NZSPO active fillers (Fig. 1e) yields a robust CSE that effectively eliminates the leakage and safety hazards inherent to liquid electrolytes. This composite architecture not only enhances ionic conductivity but also significantly improves interfacial compatibility with electrodes. This work thus establishes a versatile synthesis paradigm, combining multi-material polymerization with active filler doping to develop high-performance CSEs, and provides fundamental insights into the Na^+ diffusion mechanism, offering a promising path toward scalable solid-state sodium batteries.

Results and discussion

The synthesized free-standing electrolyte film (Fig. 1b) was fabricated through homogeneous blending of the ring-opening reaction between PAN and EPD and then mixed with a certain amount of NZSPO as the inorganic filler, forming the final composite solid electrolyte film (PPD-x, x = 0, 5, 10, 15 and 20 wt%). These films exhibit tunable thickness, a highly cross-linked feature and remarkable flexibility. Typically, PPD-10 demonstrated enhanced ionic conductivity and mechanical strength compared to its unfilled counterpart. The morphological evolution and microstructural characteristics of these CSE films were systematically probed by scanning electron microscopy (SEM) coupled with energy-dispersive X-ray spectroscopy (EDS) in Fig. 1f, g and S2b. The pristine PAN electrolyte exhibits a smooth and transparent morphology. Upon introducing the EPD component derived from ring-opening polymerization, the originally flat surface transforms into a distinctive three-dimensional network architecture. This structural reorganization not only strengthens the mechanical integrity of the electrolyte but also facilitates more uniform stress distribution during sodium plating/stripping. The successful incorporation of EPD is further confirmed by the detected oxygen signal in EDS analysis. Elemental mapping reveals a more concentrated nitrogen distribution in pure PAN, whereas PPD-0 shows a relatively diluted profile, consistent with the molecular structure of PD, where nitrogen is confined to the terminal amine groups. In the PPD-10 composite, NZSPO particles with sub-micron dimensions are uniformly dispersed throughout the polymer matrix without noticeable agglomeration. This homogeneous filler distribution is critical for establishing continuous ion-conduction pathways and ensuring

spatially consistent mechanical properties, thereby effectively suppressing localized sodium deposition and enhancing interfacial stability.

The crystalline structures of the CSE films were examined by X-ray diffraction (XRD), as shown in Fig. 1h. No discernible NZSP diffraction peaks were detected at the low filler loadings (≤5 wt%), suggesting effective shielding by the polymer matrix or highly dispersed filler distribution. Distinct crystalline peaks corresponding to the NZSP phase emerged when the filler content reached 10 wt%, and the intensity of PPD-*x* progressively increased with higher NZSPO concentrations, confirming the successful and tunable incorporation of the inorganic phase. In contrast, the XRD patterns of PAN and PPD-0 were nearly not identical, indicating the amorphous nature of the cross-linked polymer network formed by the reaction of PEGDE and PD, which lacks long-range structural order.[56]

To gain deeper insight into the chemical structure and surface morphology of the electrolyte systems, we performed Fourier-transform infrared (FT-IR) spectroscopy and atomic force microscopy (AFM). The FT-IR spectra (Fig. 2a) of PAN, PPD-0, and PPD-10 reveal key functional groups: characteristic peaks at 2230 cm^{-1} and 2921 cm^{-1} are assigned to the –C≡N stretching vibration and the asymmetric $–CH_2–$ stretching, respectively. New absorption bands emerge in the spectra of PPD-0 and PPD-10 at 1010 cm^{-1} (–C–O–C– stretching), 1350 cm^{-1} and 1373 cm^{-1} ($–CH_3$ bending), and 2865/2970 cm^{-1} (symmetric/asymmetric $–CH_3$ stretching), confirming the successful ring-opening reaction between PEGDE and DP. Notably, the FT-IR profiles of PPD-0 and PPD-10 are nearly identical, indicating that the incorporation of NZSP does not alter the chemical structure of the polymer matrix.

AFM topography images (Fig. 2b, c, and S3) further illustrate the effect of NZSPO filler incorporation. Both PPD-0 and PPD-10 films show uniform thickness without phase separation, confirming good structural integrity. Quantitative analysis indicates that the incorporation of NZSPO leads to a modest increase in surface roughness, with R_a and R_q values rising from 24.2 nm and 29.8 nm for PPD-0 to 27.7 nm and 33.6 nm for PPD-10, respectively. This minor change in roughness ($\Delta R_a = 3.5$ nm, $\Delta R_q = 3.8$ nm) suggests that the NZSPO particles are well-dispersed within the polymer host, inducing only limited topographical variation while preserving the overall structural continuity of the CSE films.[57,58]

The mechanical properties of the solid electrolytes were further evaluated by tensile testing. As shown in Fig. 2d, both PPD-0 and PPD-10 exhibit high tensile strengths of 14.26 MPa and 18.01 MPa, respectively, significantly surpassing that of pure PAN (typically 8–12 MPa), albeit with limited strain at break (<10%). This notable enhancement originates from the synergistic effect of chemical cross-linking and filler reinforcement: the ring-opening polymerization creates a robust cross-linked network in PPD-0, facilitating efficient stress distribution, while the incorporated NZSPO fillers in PPD-10 further strengthen interfacial interactions and restrict polymer chain slippage. The substantially improved mechanical robustness effectively suppresses sodium dendrite penetration, contributing to enhanced interfacial stability in solid-state sodium batteries. Furthermore, owing to the intrinsic thermal stability of the PAN backbone, the PPD-10 composite maintains excellent structural integrity after annealing at 120 °C for 30 minutes, showing no signs of deformation or degradation (Fig. S4).

The electrochemical properties of electrolytes with varying NZSPO contents were then systematically evaluated to identify the optimal composition. As depicted in Fig. 2e, the pristine PAN membrane shows a relatively low ionic conductivity of $\sim 10^{-5}$ S cm^{-1} at 30 °C. The conductivity increases progressively with NZSPO content, reaching a maximum of 1.1×10^{-4} S cm^{-1} at 10 wt% filler loading. However, beyond this optimal point, further addition of NZSPO leads to a clear decline in conductivity, which may be attributed to particle agglomeration that disrupts continuous-ion transport pathways. Furthermore, in order to verify the effect of the active filler NZSPO, we used inorganic fillers (Al_2O_3 and SiO_2) as the fillers and prepared two types of composite solid electrolytes for comparison. As shown in Fig. S5, the ionic conductivity at room temperature of the electrolyte prepared based on NZSPO was significantly higher than that of the electrolytes based on Al_2O_3 and SiO_2. This indicates that the addition of NZSPO is not a simple physical effect (suppressing polymer crystallization), but a chemical/active effect. To gain deeper insight into the ion transport mechanism, we have systematically supplemented temperature-dependent studies. Measurements were conducted across a temperature range of 25, 30, 40, 50, 60, 70, 80, and 90 °C, and the corresponding Arrhenius plot ($\log(\sigma T)$ *vs.* $1000/T$) was constructed (Fig. S6). Fitting of the linear region yielded an apparent activation energy (E_a) for ion transport of approximately 7.23 kJ mol^{-1}. This relatively low activation energy indicates a reduced energy barrier for sodium ion migration within this composite electrolyte, suggesting a facilitated transport process. This finding further confirms that the incorporation of fillers (PAN and NZSPO) not only enhances room-temperature conductivity but also effectively optimizes the thermodynamic pathway for ion transport by suppressing polymer crystallization and constructing fast interfacial channels.

The electrochemical stability of the electrolytes was assessed by linear sweep voltammetry (LSV). The electrochemical stability window (ESW) of PPD-10 is approximately 4.6 V (Fig. S7). This value is obtained by subtracting the initial oxidation potential (4.7 V) from the initial reduction potential (0.1 V), indicating its compatibility with high-voltage cathode materials. Considering that the overall reduction potential is relatively low (less than 0.1 V), the upper limit of the oxidation potential is used to distinguish the superior performance of the electrolyte with different doping contents of NZSPO. As shown in Fig. 2f, the anodic stability of pristine PAN is limited to approximately 4.2 V, whereas the incorporation of NZSPO significantly suppresses oxidative decomposition. Based on the optimal combination of ionic conductivity and electrochemical stability, the composition with 10 wt% NZSPO (PPD-10) was selected for further investigation.

The Na^+ transference number (t_{Na^+}) of PPD-10 was determined by combining potentiostatic polarization with electrochemical impedance spectroscopy (EIS) in a symmetric Na|PPD-

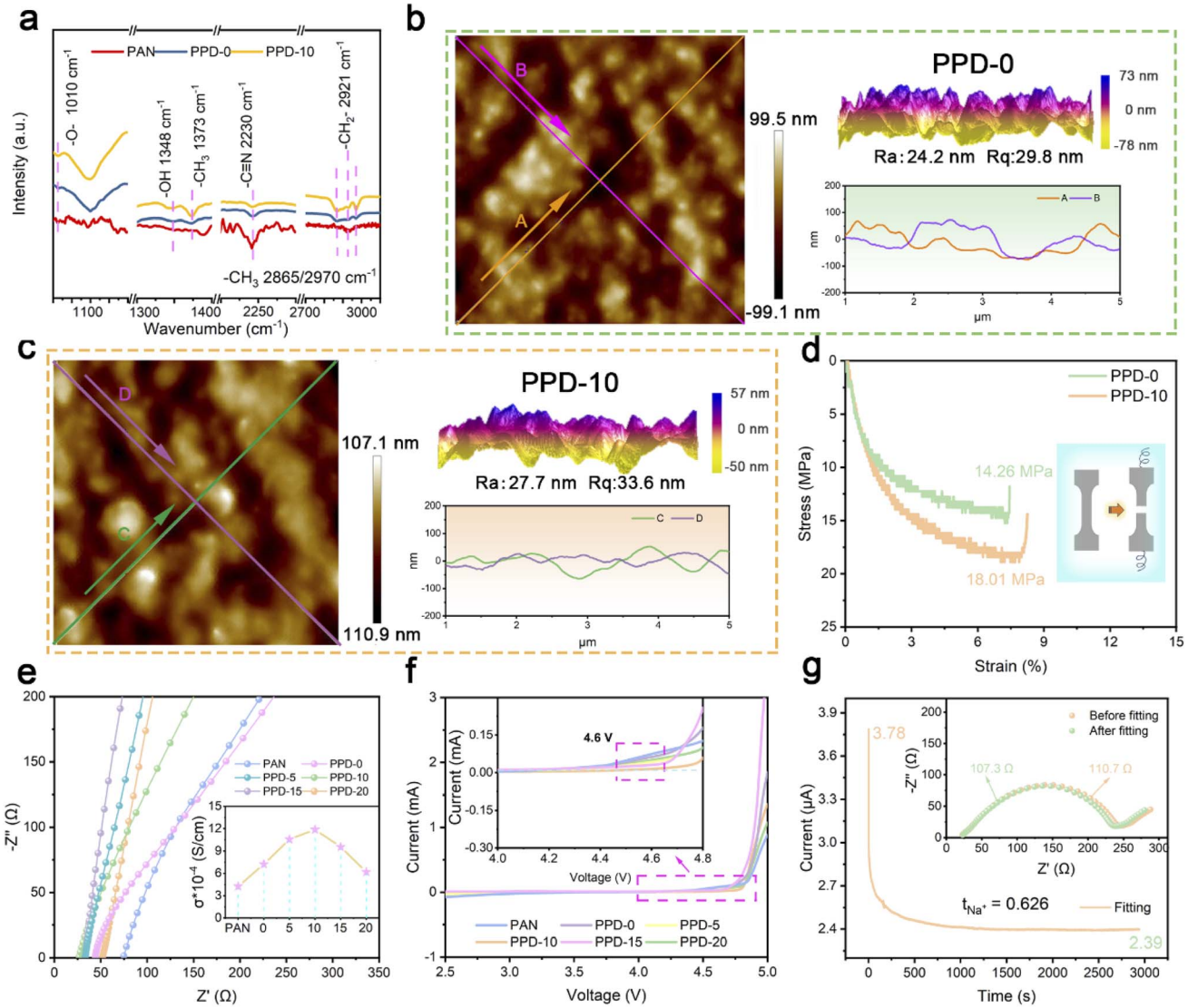

Fig. 2 Characterization of the fabricated CSE films. (a) FT-IR spectra of PAN (raw material), PPD-0 and PPD-10. AFM images of (b) PPD-0 and (c) PPD-10 with the thickness feature and 3D isopleth distribution diagram. (d) Stress–strain curves of PPD-0 and PPD-10 films. (e) EIS tests and (f) electrochemical window tests of CSE films. (g) DC polarization results for the Na|PPD-10|Na symmetrical battery at 10 mV s^{-1} and EIS variation (inset in (g)) before and after polarization.

10|Na cell (Fig. 2g). The minimal change in interfacial resistance and rapid current stabilization during polarization indicate facile Na^+ migration and stable interface characteristics. The calculated t_{Na^+} value for PPD-10 reaches 0.626, substantially higher than those of PPD-0 and pure PAN (Fig. S8). This enhancement originates from multiple synergistic effects: the polar functional groups introduced by the EPD chains provide additional coordination sites for Na^+, thereby facilitating cation transport, while the cross-linked network between EPD and PAN effectively restricts anion mobility through spatial confinement. Moreover, the introduction of NZSPO fillers creates preferential Na^+ conduction pathways at the polymer–ceramic interfaces, collectively contributing to the superior ion-transport selectivity of the composite electrolyte.

To comprehensively evaluate the electrochemical performance of the composite solid electrolyte, symmetric cells were assembled and measured the critical current density (CCD), rate performance, and long-term cyclability. As shown in Fig. 3a, the PPD-10 electrolyte enables a high CCD of 1.5 mA cm^{-2}, substantially exceeding that of PPD-0 (1.1 mA cm^{-2}, Fig. S9), and demonstrates significantly improved polarization behavior and resistance to soft short circuits. Under rate performance testing (Fig. 3b), the polarization voltage of the PPD-10-based cell increases modestly from 9 mV to 48 mV as the current density rises from 0.05 to 0.2 mA cm^{-2}. In contrast, the cell with PPD-0 exhibits a more pronounced voltage increase from 13 mV to 82 mV under the same conditions. For the long-term cycling measurement, the PPD-10 cell maintains stable operation for over 2500 hours at 0.2 mA cm^{-2} with a consistent polarization

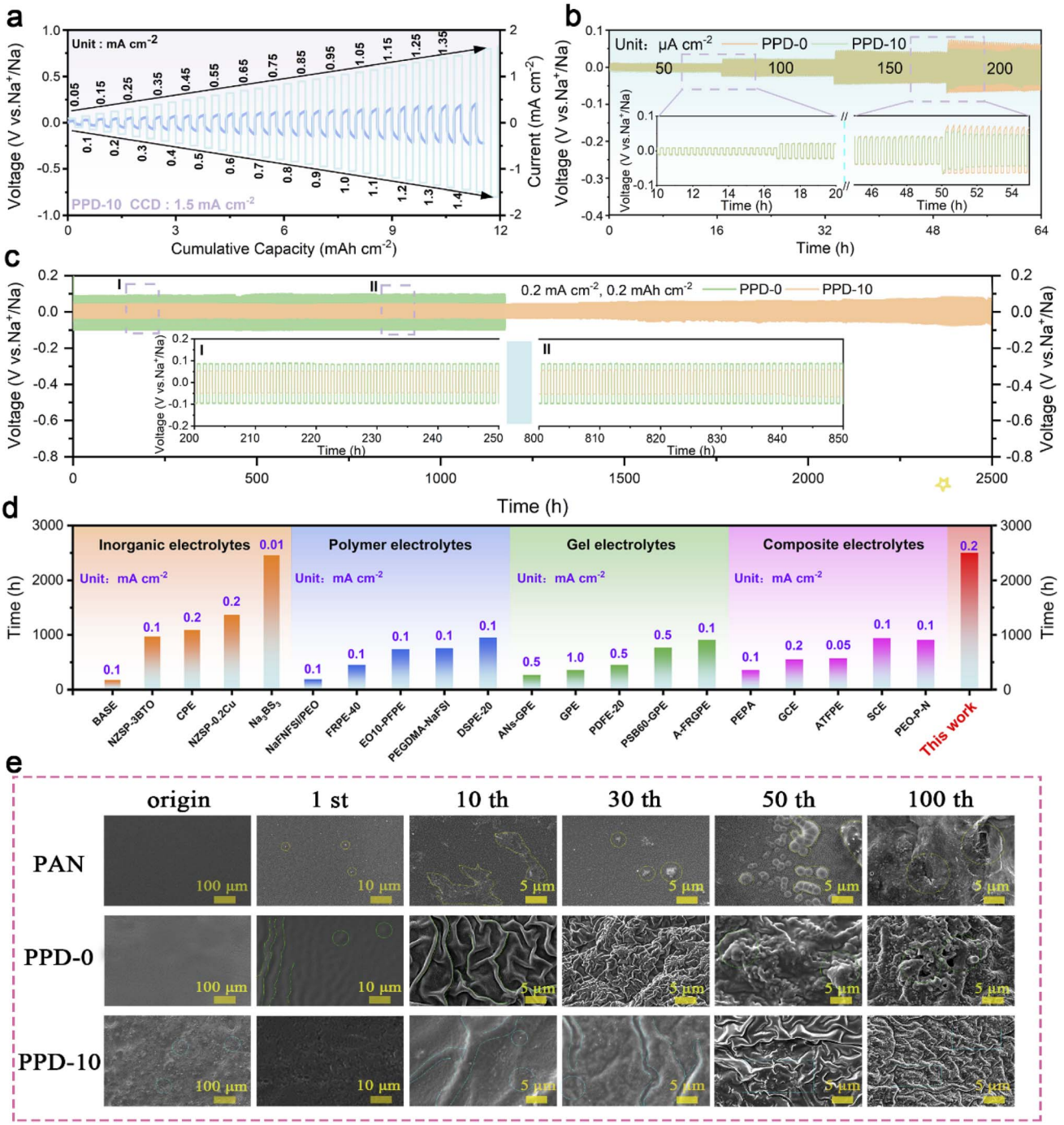

Fig. 3 The electrochemical performance of symmetric batteries. (a) CCD tests of Na|PPD-10|Na symmetric cells. (b) Rate performance of Na|PPD-0/10|Na cells from 50 to 200 μA cm^{-2}. (c) Long-term plating/stripping profiles of Na|PPD-0/10|Na cells in 0.2 mA cm^{-2} and 0.2 mAh cm^{-2}. (d) Cyclability comparison of this work and previous reported cells with various electrolytes. (e) Comparison of SEM morphologies of PAN, PPD-0 and PPD-10 films at different cycles.

voltage of ~63 mV (Fig. 3c), whereas the PPD-0 cell suffers from continuous voltage polarization growth, reaching 0.1 V after 1000 hours, followed by rapid performance decay. More critically, galvanostatic cycling tests of Na symmetric cells at 0.2 mA cm^{-2} further confirmed that the overpotential for the inert filler systems (Al_2O_3 and SiO_2) was markedly higher than that of the NZSPO system, alongside inferior stability (Fig. S10). These control experiments quantitatively prove that while all nanofillers possess some ability to inhibit polymer crystallization (a physical plasticizing effect), it is the unique high intrinsic ionic conductivity of NZSPO and the low-energy-barrier synergistic interface it forms with the polymer matrix (*i.e.*, the active conduction pathways) that are the decisive factors for achieving the high performance reported in this work. This cycling

durability of PPD-10 surpasses most reported solid electrolytes, including inorganic, polymeric, gel, and composite systems (see Table S1 for detailed comparison).

The performance hierarchy, PPD-10 > PPD-0 > PAN, can be understood from their respective structural features. The ring-opening reaction in PPD-0 yields a cross-linked network that improves chain flexibility and reduces the energy barrier for ion transport compared to pristine PAN. The further improvement in PPD-10 stems from the incorporation of NZSPO fillers, which not only provide additional fast ion-conduction pathways along the polymer–ceramic interfaces but also strengthen interfacial compatibility and reduce interfacial resistance. These results demonstrate the great potential of PPD-10 as a high-performance solid electrolyte for stable sodium-metal batteries.

To investigate the interfacial stability of composite solid electrolytes, morphology evolution of cycled symmetric cells with PPD-10, PPD-0, and PAN-based electrolytes was investigated from the original state to the 100th cycle at 0.1 mA cm^{-2} (Fig. 3e). After 50 and 100 cycles at 0.1 mA cm^{-2} (Fig. 3e), distinct differences in surface degradation were observed among the three electrolytes. The PAN-based electrolyte suffered from severe structural failure, exhibiting deep cracks, extensive grooves, and evident dendrite penetration after just 50 cycles. These defects further propagated after 100 cycles, resulting in a roughened surface with expanded cracks—a consequence of its rigid polymer chains and inadequate ion transport, which collectively exacerbate local stress concentration during repeated plating/stripping. In contrast, PPD-0 maintained improved interfacial integrity, retaining a relatively smooth surface with only shallow grooves after 50 cycles. However, localized cracks and protrusions emerged upon extended cycling to 100 cycles, indicating that the ring-opening polymerization-induced flexibility only partially alleviates mechanical stress. Remarkably, PPD-10 retained excellent interfacial compatibility throughout the cycling test. Even after 100 cycles, its surface remained largely intact with only minor, shallow grooves and no detectable dendrites, demonstrating outstanding interfacial resilience. This hierarchy in interfacial stability originates from the distinct structural design of each electrolyte. The pure PAN electrolyte, with its rigid chains and poor ionic transport, leads to progressive interfacial failure. The cross-linked network in PPD-0 improves flexibility and stress dissipation but remains insufficient for long-term cycling. PPD-10, however, achieves exceptional stability through a synergistic combination of a flexible polymer matrix and well-dispersed NZSPO fillers. The former enhances chain mobility and ion transport, while the latter reinforces mechanical strength, reduces interfacial resistance, and promotes uniform ion flux. This multi-scale design effectively suppresses dendrite initiation and propagation, underscoring the promise of PPD-10 for high-performance solid-state sodium batteries.

X-ray photoelectron spectroscopy (XPS) was employed to probe the chemical states and interfacial interactions within the composite electrolytes. As shown in Fig. 4a, the core-level spectra of C 1s, N 1s, and O 1s all exhibit noticeable shifts upon NZSPO incorporation, accompanied by a significant reduction in binding energy. For instance, the binding energies of C–C/C–H, N–C, and O–H bonds shift from 285.2, 399.2, and 534.0 eV in PPD-0 to 283.8, 398.2, and 532.8 eV in PPD-10, respectively. These systematic shifts suggest strong interfacial coupling between the polymer matrix and NZSPO filler, which likely modifies the local electron density and reduces the energy barrier for charge transfer. In the N 1s spectrum (Fig. 4a-2), the binding energy of the N–H group decreases from 398.6 eV in the precursor to 398.2 eV after ring-opening polymerization, attributable to the electron-withdrawing effect of the adjacent hydroxyl group and the possible formation of intramolecular hydrogen bonds. Furthermore, the absence of the characteristic cyclic C–O–C peak at 532.8 eV confirms the complete ring-opening reaction between PEGDE and PD. The appearance of a distinct NZSPO-related peak at 529.2 eV in the O 1s spectrum of PPD-10 (Fig. 4a-4) provides direct evidence for the successful integration of the inorganic filler into the polymer composite.

To elucidate the ion-transport mechanisms, density functional theory (DFT) calculations were performed. As illustrated in Fig. 4b, Na^+ migration in PPD-10 follows a hierarchical pathway involving both the polymer matrix and the ceramic filler. Within the polymer phase (Fig. 4c), the PEGDE-PD cross-linked network in PPD-0 reduces the Na^+ migration barrier to 0.66 eV, a 26% decrease compared to pristine PAN (0.89 eV). This enhancement stems from two synergistic effects: the formation of continuous amorphous domains and the restriction of polymer segmental motion, which collectively shift-ion transport from chain-assisted hopping to a more efficient vehicular diffusion mode.

Furthermore, Na^+ preferentially adsorbs at site C (octahedral coordination), with metastable sites A and B located 0.19 eV higher in energy on the NZSPO surfaces (Fig. 4d). The most favorable surface diffusion path follows the sequence C → B → A → C with an energy barrier of 0.82 eV, significantly lower than the reverse C → A → B pathway (0.89 eV). More importantly, bulk diffusion through the NZSPO lattice dominates over surface transport, as evidenced by the low energy barrier of 0.33 eV for Na^+ migration from the surface to subsurface sites. Within the bulk lattice (Fig. 4e), Na^+ ions occupy two distinct sites: the regular octahedral Na_6 and the distorted Na_8 with 6–8 coordination. The optimal bulk conduction route Na_6 → Na_6 → Na_8 → Na_6 → Na_6 is identified, with low transition barriers between Na_6 and Na_8 sites (0.19 eV and 0.15 eV, respectively) compared to the high-energy Na_8 → Na_8 hop (0.63 eV). Furthermore, the migration energy barriers for the two-phase process of the organic phase and the inorganic phase were also calculated, and the result was 0.75 eV (Fig. S11), which was smaller than that of a single polymer chain (>1.0 eV). Compared with the energy of the three parts of the region calculated previously, it is not much higher either. It does not become a key factor restricting the Na transport, ensuring the rapid transport of Na within the system. This hierarchical transport system—combining optimized polymer-filler interfaces with efficient bulk and polymer-phase conduction—collectively enhances the room-temperature ionic conductivity by two orders of magnitude relative to conventional PAN-based electrolytes, providing a fundamental understanding of the superior performance of PPD-10 in solid-state sodium batteries.

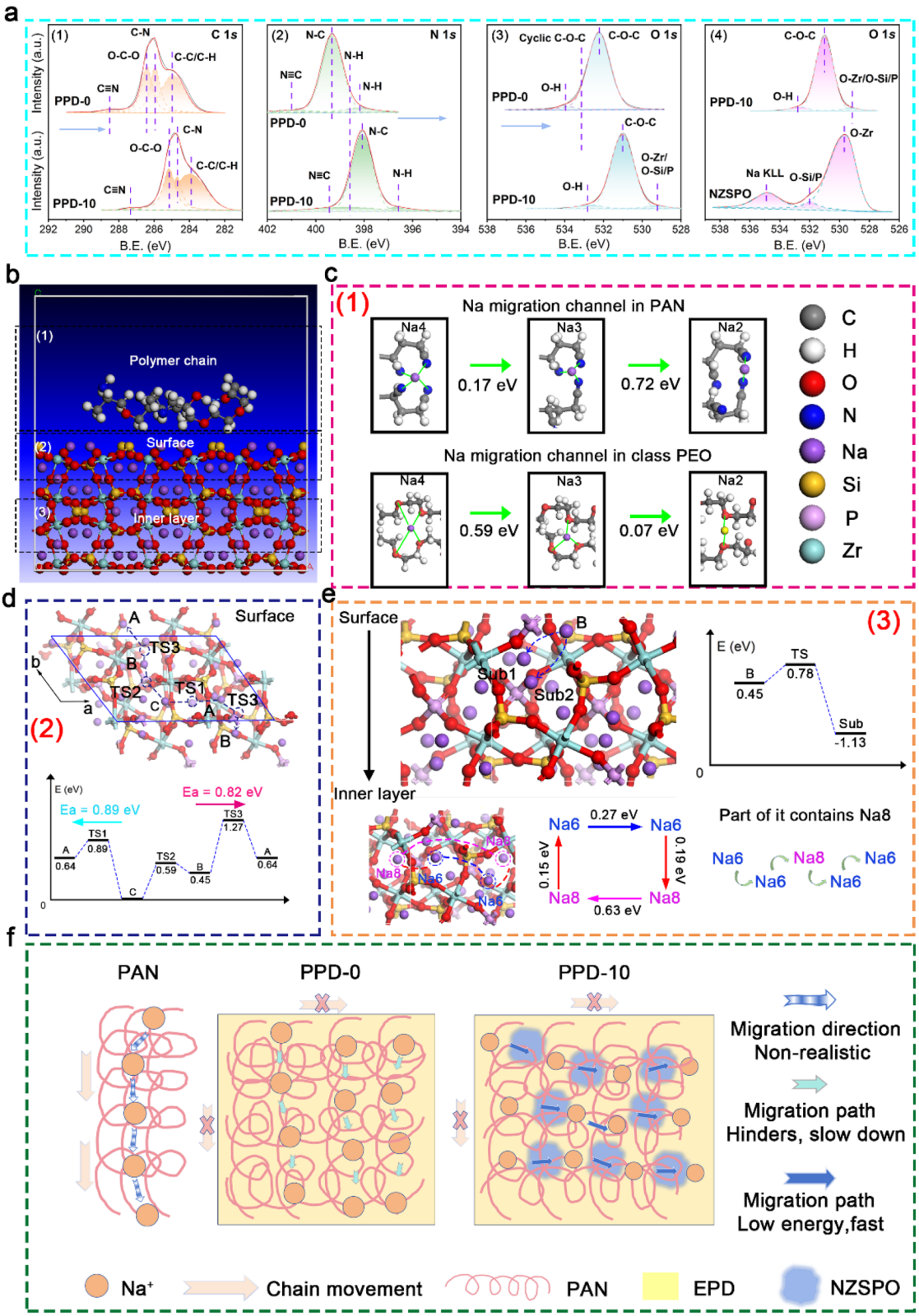

Fig. 4 (a) High-resolution XPS analysis of C 1s, N 1s, and O 1s spectra for PPD-0, PPD-10 and NZSPO. (b) Typical three transmission paths of Na^+ ions in the composite solid-state electrolyte: polymer chain, interface, and inner layer. (c) The Na^+ transport pathway with barriers from site to site in PAN chains and PEGDE/PD. (d) The mechanism and free energy profiles for Na migration on the surface of NZSPO. (e) The mechanism and free energy for Na diffusing from the surface to the inner layer of NZSPO. (f) Schematic diagram of the Na^+ migration mechanism for PAN, PPD-0 and PPD-10.

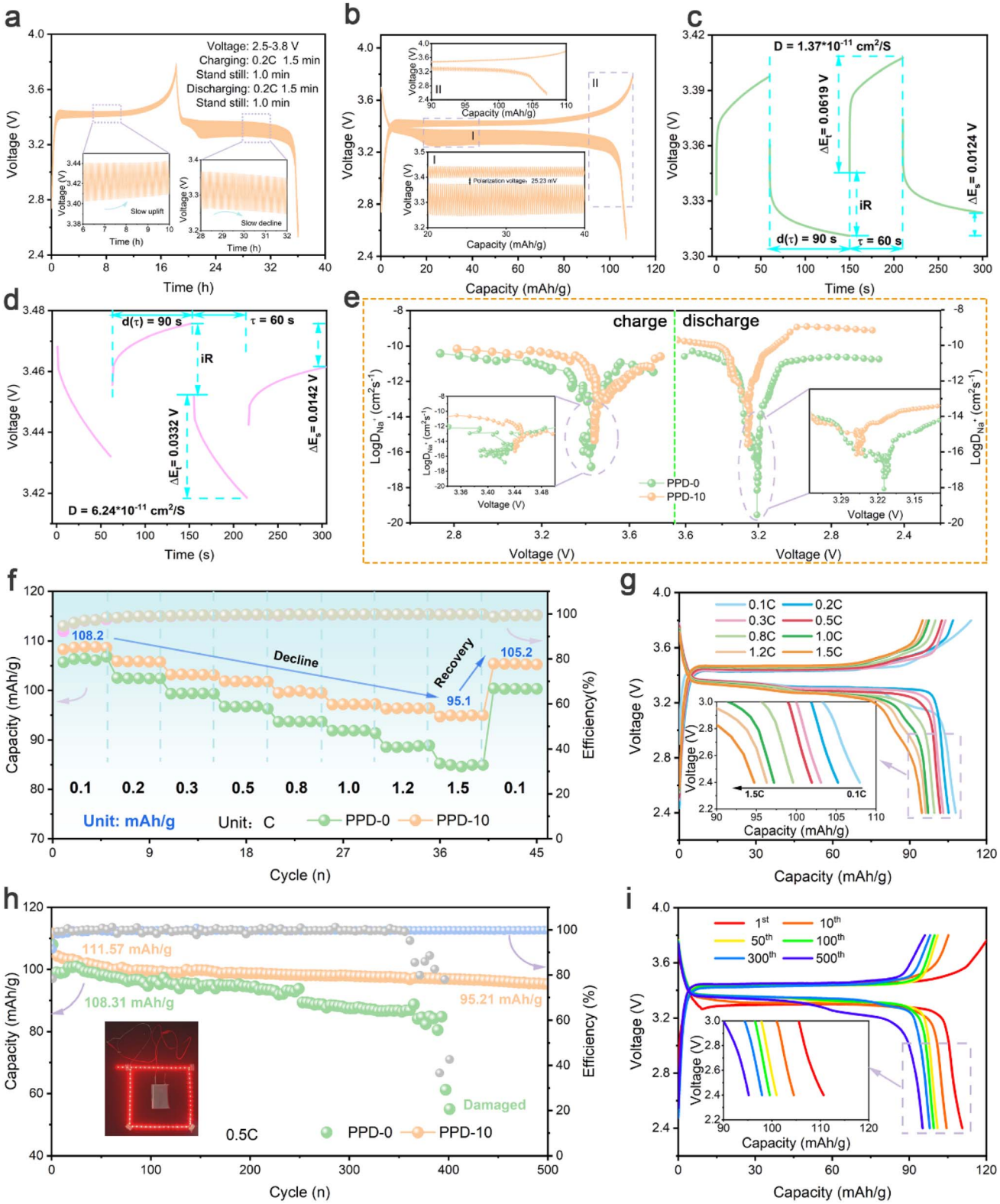

Fig. 5 GITT test of Na|PPD-10|NVP batteries: (a) time–voltage profile. (b) Charge and discharge profiles of capacity and voltage. (c and d) Time–voltage profile for a specific time point. (e) Comparison of Na^+ diffusion coefficients between PPD-0 and PPD-10; (f) rate performance of Na|PPD-0/10|NVP batteries. (g) Galvanostatic charge–discharge voltage profiles of Na|PPD-10|NVP batteries at different rates. (h) Cycling performances of Na|PPD-0/10|NVP batteries at 0.5C (inset: the light-emitting diode powered by the pouch cell of the Na|PPD-0/10|NVP battery; soft-pack battery capacity and bulb testing). (i) Galvanostatic charge–discharge voltage profiles of Na|PPD-10|NVP batteries at different cycles.

Galvanostatic intermittent titration technique (GITT) measurements were conducted to quantify the Na^+ diffusion kinetics in the solid-state cells. As shown in Fig. 5a–c, the PPD-10-based cell exhibits significantly reduced polarization and smoother voltage transitions during the intermittent relaxation periods compared to the PPD-0 cell (Fig. S12), indicating enhanced interfacial kinetics and rapid ion transport. The Na^+ diffusion coefficients (D_{Na^+}) of PPD-10, calculated using the Weppner–Huggins equation, range from 4.22×10^{-16} to 3.82×10^{-11} cm^2 s^{-1} within the voltage window of 2.5–3.8 V (Fig. 5d and e). Notably, the maximum D_{Na^+} value occurs at 3.40 V, corresponding to the V^{4+}/V^{5+} redox reaction in the NVP cathode. Throughout the entire (dis)charge process, PPD-10 demonstrates consistently higher diffusion coefficients than PPD-0, which can be attributed to the synergistic effects of the hierarchical ion-transport pathways (as revealed by DFT), the uniform Na^+ deposition behavior (observed *via* SEM), and the high intrinsic ionic conductivity of the composite electrolyte.

The practical performance of PPD-10 was further evaluated in NVP|PPD-10|Na full cells. Under rate capability testing (Fig. 5f), the cell with PPD-10 delivered high discharge capacities of 108.2 mAh g^{-1} at 0.1C and 95.1 mAh g^{-1} at 1.5C, corresponding to a high-capacity retention of 87.9%. When the current rate is returned to 0.1C, the capacity recovers to 105.2 mAh g^{-1} (97.2% of the initial value). In contrast, the PPD-0-based cell shows a more pronounced capacity drop from 106.8 mAh g^{-1} (0.1C) to 84.3 mAh g^{-1} (1.5C), with only 93.5% recovery. The charge/discharge profiles (Fig. 5g) further confirm the superior kinetics of PPD-10, which maintains well-defined voltage plateaus even at high rates, whereas PPD-0 exhibits significant polarization.

Long-term cycling performance at 0.5C reveals exceptional stability for the PPD-10 cell (Fig. 5h and i). It retains a capacity of 95.21 mAh g^{-1} after 500 cycles, with a capacity retention of 85.3% and an average decay rate as low as 0.029% per cycle. The charge/discharge curves remain stable with minimal voltage polarization growth ($\Delta V < 0.1$ V). In comparison, the PPD-0 cell suffers from continuous capacity fading and increasing polarization ($\Delta V \approx 0.25$ V), leading to failure after ~400 cycles. To verify the performance of the PPD-10 material under high current and high active substance loading conditions, we conducted group tests on its performance, with the following conditions: 2.0C, 1.5 mg cm^{-2} (Fig. S13), 0.5C, 3.7 mg cm^{-2} (Fig. S14), and 2.0C, 3.5 mg cm^{-2} (Fig. S15). These new data confirm that the composite solid electrolyte can retain reasonably good cycling stability even under high loadings, demonstrating its practical potential. They also objectively reveal the accelerated capacity fade at ultra-high rates (*e.g.*, 2.0C), which is primarily attributed to the limitations in sodium-ion transport kinetics at the electrode/electrolyte interface at high current density. This insight points to a clear direction for future interface engineering optimization. The degradation of PPD-0 is consistent with the severe interfacial cracks observed in post-cycling SEM images (Fig. S16 and S17), whereas PPD-10 retains a relatively intact interface. When benchmarked against recently reported solid electrolytes (Fig. S18, S19 and Table S1), PPD-10 demonstrates competitive performance in terms of polarization, capacity retention, and cycling life. Moreover, a flexible pouch cell assembled with PPD-10 (Fig. S20) successfully powers a light-emitting diode (inset of Fig. 5h), demonstrating its potential for practical applications. In addition to the cycle performance, we also tested the impedance changes during the *in situ* charge and discharge process of the PPD-10 assembled all-cell battery, as well as the corresponding Distribution of Relaxation Times (DRT) analysis (Fig. S21). The results show that during charging, the total cell impedance gradually decreased, while during discharging, the impedance gradually increased, nearly recovering its initial value, indicating good reversibility. DRT deconvolutes the total impedance into processes with different time constants (τ). We observed that the intensity of the peak associated with charge transfer at the electrode–electrolyte interface ($\log(\tau) \approx -3$) weakened during charging and strengthened during discharging. This quantitatively indicates that during charging, Na^+ extraction from the cathode increases the Na^+ concentration at the interface, optimizing interfacial transport kinetics and reducing interfacial resistance. During discharging, Na^+ insertion decreases the interfacial Na^+ concentration, causing a reversible increase in resistance. This dynamic and reversible change in interfacial impedance directly proves that our composite electrolyte forms a stable and kinetically responsive interface with the electrodes, which is crucial for long-term cycling stability and a dynamic manifestation of the "synergy" during battery operation.

These results collectively highlight the effectiveness of the composite electrolyte design, which integrates ring-opening polymerization and active filler incorporation to achieve stable ion transport and durable electrode–electrolyte interfaces, rendering PPD-10 a highly promising candidate for high-energy-density solid-state sodium batteries.

Conclusion

In conclusion, through a reasonable multi-component design strategy, we successfully developed a high-performance composite solid electrolyte (PPD-10). Through the *in situ* open-loop polymerization reaction of PEGDE and DP-2000, a polymer network similar to the PEO-chain structure is generated. Then, by adding high dielectric PAN components and active filler NZSPO components, the mechanical strength of the electrolyte is improved while ensuring the conductivity performance. This unique architecture synergistically combines the advantages of each component: the cross-linked polymer matrix ensured flexibility and interfacial compatibility, while the active filler of NZSPO significantly enhanced ionic conductivity, mechanical strength, and interfacial stability. The as-fabricated PPD-10 electrolyte exhibited a high Na^+ transference number of 0.64, an outstanding ionic conductivity of $>1.2 \times 10^{-3}$ S cm^{-1} at 30 °C, and a wide electrochemical window of ~4.6 V. These superior properties collectively contribute to remarkable electrochemical performance in both symmetric and full cells, including stable sodium plating/stripping over 2500 hours and high-capacity retention in NVP/Na cells for 500 cycles. Combined experimental and theoretical analyses reveal that the

excellent performance originates from the hierarchical Na^+ transport pathways and the robust electrode–electrolyte interface enabled by the composite structure. This work not only presents a feasible strategy for designing highly conductive and interface-compatible solid electrolytes but also provides fundamental insights into the ion transport mechanisms in composite systems, providing valuable guidance for the development of next-generation solid-state sodium batteries with high energy density and enhanced safety.

Author contributions

L. Zhai and S. Chen conceived and designed the experiments. L. Zhai, H. Dong, H. Wang, Y. Duan and Z. Liu synthesized the materials and carried out the electrochemical analyses. L. Zhai, S. Yan, and C. You perform full cell assembly and testing. H. Yan and X. Tan provided manuscript revisions and suggestions. L. Zhai, X. Tan and S. Chen performed computational analyses. S. Chen supervised the work and contributed to the manuscript's revision and finalization. All the authors participated in the discussion of the research.

Conflicts of interest

The authors declare no conflict of interest.

Data availability

The data supporting this article have been included as part of the supplementary information (SI). Supplementary information: experimental section including the preparation of NZSPO, PPD-*x* electrodes, materials characterization and electrochemical measurements. See DOI: https://doi.org/10.1039/d5sc09295g.

Acknowledgements

We gratefully acknowledge the National Natural Science Foundation of China (22479115), Innovative Research Team of High-level Local Universities in Shanghai, Zhejiang Provincial Natural Science Foundation of China (LY24E020002), and Wenzhou basic scientific research project (G20240022). In addition, all the computations were performed on the high-performance computing platform of Shanghai University with official permission.

References

1 Z. C. Bai, Q. Yao, M. Y. Wang, W. J. Meng, S. X. Dou, H. K. Liu and N. N. Wang, *Adv. Energy Mater.*, 2024, **14**, 2303788.
2 C. Che, F. Wu, Y. Li, Y. Li, S. Q. Li, C. Wu and Y. Bai, *Adv. Mater.*, 2024, **36**, 2402291.
3 X. H. Liu, W. H. Lai, J. Peng, Y. Gao, H. Zhang, Z. Yang, X. X. He, Z. Hu, L. Li, Y. Qiao, M. H. Wu and H. K. Liu, *Carbon Neutralization*, 2022, **1**, 49–58.
4 Q. Liu, Q. An, K. Zeng, M. Yang, H. Zhu, X. Liang, G. Zhao, M. Sun, Y. Zha, L. Yang, L. Duan, G. Zhao, Y. Sun and H. Guo, *Energy Environ. Sci.*, 2025, **18**, 4934–4948.
5 X. X. Lan, N. Luo, Z. Li, J. Peng and H. M. Cheng, *ACS Nano*, 2024, **18**, 9285–9310.
6 S. J. Liu, L. Zhou, T. J. Zhong, X. Wu and K. Neyts, *Adv. Energy Mater.*, 2024, **14**, 2403602.
7 H. L. Luo, Z. X. Guan, C. H. Wu, Y. C. Zhu, C. Wang, X. Y. Wang, D. Y. Guo, X. A. Chen and S. Wang, *Adv. Funct. Mater.*, 2024, **34**, 2407007.
8 Q. An, Q. Liu, P. Mao, L. Duan, H. y. Zhu, L. Liu, G. Zhao, Y. Zha, L. Yang, M. Sun, Y. Fan, F. Xie, G. Hu and H. Guo, *Angew. Chem., Int. Ed.*, 2025, **64**, e202422539.
9 W. X. Zhao, H. H. Dong, Z. Xing, L. M. Zhou, S. Q. Chen, H. K. Liu, S. X. Dou, Z. W. Zhao, H. Xia, S. L. Chou and M. Z. Chen, *Adv. Energy Mater.*, 2024, **14**, 2402720.
10 S. Z. Zhao, H. Y. Che, S. L. Chen, H. X. Tao, J. P. Liao, X. Z. Liao and Z. F. Ma, *Electrochem. Energy Rev.*, 2024, **7**, 3.
11 C. J. Lou, W. D. Zhang, J. Liu, Y. N. Gao, X. Sun, J. P. Fu, Y. C. Shi, L. G. Xu, H. J. Luo, Y. J. C, X. Gao, X. J. Kuang, L. Su and M. X. Tang, *Chem. Sci.*, 2024, **15**, 3988–3995.
12 Y. Zhou, M. Hou, X. Yang, X. Zhang, H. Xiong and F. Liang, *Rev. Mater. Res.*, 2025, **1**, 100104.
13 G. Z. Liu, J. Yang, J. H. Wu, Z. Peng and X. Y. Yao, *Adv. Mater.*, 2024, **36**, 2311475.
14 Z. J. Wu, S. N. He, C. Zheng, J. T. Gan, L. N. She, M. C. Zhang, Y. Gao, Y. X. Yang and H. G. Pan, *eScience*, 2024, **4**, 100247.
15 I. A. Ojelade, E. Truong, I. P. Oyekunle, T. P. Poudel, Y. D. Chen, M. J. Deck, Y. K. Jin, B. Ogbolu, P. K. Ojha, M. M. Islam, T. N. D. D. Gamaralalage, J. S. R. V. Winfred and Y. Y. Hu, *Chem. Sci.*, 2025, **16**, 19857–19866.
16 F. Liang, S. Z. Wang, Q. Liang, A. Zhong, C. Yang, J. Qian, H. J. Song and R. J. Chen, *Adv. Energy Mater.*, 2024, **14**, 2401959.
17 W. L. Feng, Y. F. Zhao and Y. Y. Xia, *Adv. Mater.*, 2024, **36**, 2306111.
18 J. X. Zhang, J. M. Fu, P. S. Lu, G. T. Hu, S. J. Xia, S. T. Zhang, Z. Q. Wang, Z. M. Zhou, W. L. Yan, W. Xia, C. H. Wang and X. L. Sun, *Adv. Mater.*, 2025, **37**, 2413499.
19 X. Wang, Y. M. Fan, J. Y. Li, X. H. Li, W. J. Li, J. Z. Wang and W. K. Pang, *Energy Environ. Sci.*, 2025, **18**, 1096.
20 S. Rizvi, I. Aladhyani, Y. Ding and Q. F. Zhang, *Nano Energy*, 2024, **129**, 110009.
21 A. A. Bristi, A. J. Samson, A. Sivakumaran, S. Butler and V. Thangadurai, *ACS Appl. Energy Mater.*, 2022, **5**, 8812–8822.
22 W. Ling, N. Fu, J. P. Yue, X. X. Zeng, Q. Ma, Q. Deng, Y. Xiao, L. J. Wan, Y. G. Guo and X. W. Wu, *Adv. Energy Mater.*, 2020, **10**, 1903966.
23 D. Yang, H. Zhou, B. Wang, K. Ren, P. Liu, Y. Zhou, D. Zhang, S. Hou, F. Li, M. Hou, Y. Cai, H. Wu, B. Yang and F. Liang, *ACS Energy Lett.*, 2025, **10**, 4777–4786.
24 K. Ren, H. Zhou, D. Zhang, D. Yang, F. Li, X. Zhang, P. Liu, Y. Zhou, P. Dong, X. Feng, H. Wu, K. Hayashi, B. Yang and F. Liang, *Adv. Energy Mater.*, 2025, **15**, e00472.
25 K. Noi, Y. Nagata, T. Hakari, K. Suzuki, S. Yubuchi, Y. Ito, A. Sakuda, A. Hayashi and M. Tatsumisago, *ACS Appl. Mater. Interfaces*, 2018, **10**, 19605–19614.

26 N. N. Zhang, H. X. Di, B. H. Wen, J. Y. Luo, L. Zhang and S. J. Zhang, *Nano Energy*, 2024, **130**, 110175.
27 A. Yang, K. Yao, M. Schaller, E. Dashjav, H. Li, S. Zhao, Q. Zhang, M. Etter, X. C. Shen, H. M. Song, Q. Q. Lu, R. J. Ye, I. Moudrakovski, Q. Q. Pang, S. Indris, X. C. Wang, Q. L. Ma, F. Tietz, J. Chen and Q. Guillon, *eScience*, 2023, **3**, 100175.
28 A. Nasu, T. Inaoka, F. Tsuji, K. Motohashi, A. Sakuda, M. Tatsumisago and A. Hayashi, *ACS Appl. Mater. Interfaces*, 2022, **14**, 24480–24485.
29 Q. Wang, Z. L. Jiang, C. Yu, L. P. Li and G. S. Li, *Chin. Chem. Lett.*, 2025, **36**, 110006.
30 Z. L. Dong, Y. Gan, V. Martins, X. Wang, B. Fu, E. Jin, Y. Gao, Y. Hu, X. Lin, Y. Yuan, C. Turner, X. Pang, H. Abdolvand, Y. Huang, T.-K. Sham and Y. Zhao, *Adv. Mater.*, 2025, **37**, 2503107.
31 J. H. Guo, F. Feng, X. Y. Jiang, R. Wang, D. K. Chu, Y. F. Ren, F. F. Chen, P. He, Z. F. Ma, S. L. Chen and T. X. Liu, *Adv. Funct. Mater.*, 2024, **34**, 2313496.
32 L. Shen, S. G. Deng, R. R. Jiang, G. Z. Liu, J. Yang and X. Y. Yao, *Energy Storage Mater.*, 2022, **46**, 175–181.
33 S. L. Chen, H. Y. Che, F. Feng, J. P. Liao, H. Wang, Y. M. Yin and Z. F. Ma, *ACS Appl. Mater. Interfaces*, 2019, **11**, 43056–43065.
34 Z. Zhang, Y. Huang, C. Li and X. Li, *ACS Appl. Mater. Interfaces*, 2021, **13**, 37252–37262.
35 G. Yang, M. L. Lehmann, S. Zhao, B. R. Li, S. R. Ge, P. F. Cao, F. M. Delnick, A. P. Sokolov, T. Saito and J. Nanda, *Energy Storage Mater.*, 2021, **35**, 431–442.
36 E. Ruoff, S. Kmiec and A. Manthiram, *Small*, 2023, **20**, 2311839.
37 X. J. Tang, W. B. Han, Y. Zhang and S. Liu, *J. Power Sources*, 2024, **623**, 235397.
38 Y. Fan, Y. Feng, G. Li, Y. Bo, C. Wang, D. Wang, Y. Qian, R. Ma, Z. Hu, K. Zhang and J. Chen, *Adv. Mater.*, 2024, **36**, 2413303.
39 J. Y. Hou, T. K. Zhu, G. Wang, R. Cheacharoen, W. Sun, X. Y. Lei, Q. Y. Yuan, D. L. Sun and J. Zhao, *Carbon Energy*, 2024, **6**, e628.
40 S. Kmiec, E. Ruoff, J. Darga, A. Bodratti and A. Manthiram, *ACS Appl. Mater. Interfaces*, 2023, **15**, 20946–20957.
41 Y. X. Guo, J. C. Liu, A. H. Shao, L. Cheng, J. W. Tang, Y. X. Zhang, Z. Q. Wang, Y. S. Li, Y. C. Wang, H. L. Wang, C. W. Li, T. Liu, X. D. Zhao and Y. Ma, *Adv. Energy Mater.*, 2024, **15**, 2405104.
42 W. Zhang, T. Xiong, Z. Bai, H. Liu and X. Qiu, *Electrochem. Energy Rev.*, 2025, **8**, 33.
43 X. Liu, X. Dai, Q. Lin, Y. Li, D. Liu, Z. Xiao, L. Liu, Z. Qian and R. Wang, *Small*, 2025, 2501133.
44 X. J. Zhang, X. C. Wang, S. Liu, Z. L. Tao and J. Chen, *Nano Res.*, 2018, **11**, 6244–6251.
45 Z. Sun, Y. Zhao, Q. Ni, Y. Liu, C. Sun, J. Li and H. Jin, *Small*, 2022, **18**, 2200716.
46 J. Guo, F. Feng, S. Zhao, R. Wang, M. Yang, Z. Shi, Y. Ren, Z. Ma, S. Chen and T. Liu, *Small*, 2023, **19**, 2206740.
47 L. Ran, S. Tao, I. Gentle, B. Luo, M. Li, M. Rana, L. Wang and R. Knibbe, *ACS Appl. Mater. Interfaces*, 2021, **13**, 39355–39362.
48 B. Zhou, C. Yang, F. Wu, T. Deng, S. Guo, G. Zhu, Y. Jiang and Z. Wang, *Chem. Eng. J.*, 2022, **450**, 138385.
49 G. Åvall, J. Mindemark, D. Brandell and P. Johansson, *Adv. Energy Mater.*, 2018, **8**, 1703036.
50 E. Ruoff, S. Kmiec and A. Manthiram, *Adv. Energy Mater.*, 2024, **14**, 2402091.
51 L. Yang, L. Wang, Q. Hu, M. Yang, G. Zhao, Y. Zha, Q. An, Q. Liu, H. Xie, Y. Sun, L. Duan, X. Zou, G. Zhao and H. Guo, *Energy Storage Mater.*, 2025, **77**, 104210.
52 P. Liu, F. Li, K. Ren, M. Hou, D. Yang, X. Yang, X. Wang, Y. Lei and F. Liang, *Nano Energy*, 2026, **148**, 111637.
53 S. L. Wu, Z. F. Yu, X. L. Nie, Z. H. Wang, F. L. Huang and Q. F. Wei, *Adv. Energy Mater.*, 2022, **12**, 2202930.
54 E. J. Kim, P. R. Kumar, Z. T. Gossage, K. Kubota, T. Hosaka, R. Tatara and S. Komaba, *Chem. Sci.*, 2022, **13**, 6121–6158.
55 X. W. Yu, L. G. Xue, J. B. Goodenough and A. Manthiram, *Adv. Funct. Mater.*, 2021, **31**, 2002144.
56 Z. Y. Wang, Z. W. Wu, Q. Ma, J. Zhou, Q. Zhang, K. H. Yu, P. Lv and W. Wei, *Chem. Eng. J.*, 2024, **500**, 156722.
57 K. Li, Q. R. Du and Y. Gong, *Chem. Eng. J.*, 2024, **500**, 157104.
58 W. T. Wang, M. H. Ding, S. Y. Chen, J. Y. Weng, P. J. Zhang, W. Y. Yuan, A. J. Bi and P. F. Zhou, *Chem. Eng. J.*, 2024, **491**, 151989.